# RTS Noise in CMOS Image Sensors Irradiated with High Energy Photons

Ben Hendrickson, Ralf Widenhorn, Morley Blouke, *Lifetime Member, IEEE*, Denis Heidtmann, and Erik Bodegom

***Abstract*--This paper explores the phenomenon of dark current random telegraph signal (DC-RTS) noise in commercial off-the-shelf CMOS image sensors. Five sensors were irradiated with high energy photons to a variety of doses and analyzed with a wavelets-based signal reconstruction algorithm. The algorithm is explained in detail, and the radiation effects on individual pixels are discussed. Finally, the generation rate of RTS pixels as a function of dose is explored, providing information on the underlying defect structure responsible for this noise source.**

***Keywords*—CMOS image sensor, dark current random telegraph signal (DC-RTS), wavelet transform, denoising, gamma irradiation, 2nd order defect generation**

## I - INTRODUCTION

RANDOM Telegraph Signal (RTS) noise is characterized by discrete transitions in the signal current of a MOSFET device (see Figure 1). Studied since the 1960s [1], the steady shrinking of pixel pitch has driven RTS noise to become a major noise source in modern CMOS image sensors. These transitions occur due to alterations in the conductivity $\sigma$, which is expressed as $\sigma = \mu n q$ where $\mu$ is the mobility across the channel, $n$ is the number of charge carriers, and $q$ is the fundamental charge. RTS is known to have two primary causes, a change in $\mu$ brought on by the trapping/emission of a charge carrier in the gate oxide, and a change in $n$ which arises from a metastable Shockley-Read-Hall (SRH) generation and recombination (G/R) center [2],[3].

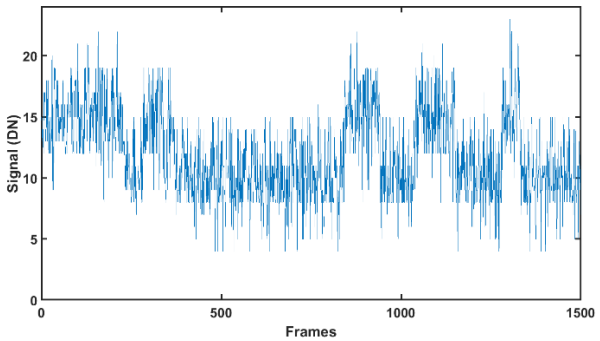


**Figure 1:** A prototypical bi-stable RTS-Noise Signal

The authors are with Portland State University, Portland Oregon, USA

With regards to a CMOS image sensor, the change in mobility can occur in the source follower transistor, which acts as an amplifier for the charge induced by exposure to photons or dark current. As such, this flavor of RTS is called Source Follower RTS, or SF-RTS. If a charge becomes trapped in the gate oxide, the gate-source voltage $V_{gs}$ is lowered, which decreases the mobility across the channel. Once the trapped charge is emitted, $V_{gs}$ returns to its normal operating value and the signal again reads true, exempting of course other noise sources.

The physical mechanism behind the change in $n$ is still inconclusive, but is likely to occur from the turning on and off of SRH G/R centers in the depleted region of a photodiode or on the $Si/SiO_2$ interface touching the photodiode. Reported activation energies around the mid-gap level ($\sim 0.56eV$) supports metastable SRH G/R as the mechanism behind this second type of RTS [4],[5]. There is some variance in these measurements, so it is conceivable that a metastable bond rotation would change a trap state energy to be closer or further away from the center of the band gap, creating the conditions necessary to produce the observed signal. Or, perhaps a charge trap located on the boundary of the space charge region would move the depletion edge depending if it was in the capture or emission state. Regardless, this noise source is differentiated from SF-RTS by its very long state lifetimes [8], and the fact that the RTS amplitude is a function of integration time. Since the form of RTS noise changes the dark current level in a pixel by a discrete amount, it has been denoted as Dark Current RTS (DC-RTS) [9].

DC-RTS has been studied for over a decade [4]-[10], and the current state of the art technique for characterization was developed by V. Goiffon et. al. in the late 2000's [9]. This method convolves a step shaped filter with signals of interest to detect RTS and extract both the various levels and state lifetimes. Here, we report a study of RTS and how the phenomenon depends on radiation from high energy photons including evidence for $2^{nd}$ order defect generation. Rather than convolution, we explore if a method based on wavelet denoising, or shrinkage can be utilized. Wavelets are ubiquitous in image and signal processing [11]-[15] today, but have been little used in RTS studies. The following sections provide a brief outline of the mathematics behind wavelet denoising, and a detailed explanation of the wavelets denoising process that was used in this study.

## II - EXPERIMENTAL INVESTIGATION OF DC-RTS NOISE

As stated previously, DC-RTS is a noise source characterized by a discrete change in the dark current of a pixel, identified by integration time dependence on RTS amplitude and time constants which are characteristically much longer than source follower RTS (SF-RTS). What remains elusive is the mechanism behind this noise source.

In order to study characteristics of DC-RTS amplitudes and time constants, five commercial-off-the-shelf Omnivision OV5647 CMOS image sensors were irradiated at the Oregon Health & Science University Radiation Medicine department. These sensors were used, among others, in the iPhone 4 and in the Raspberry Pi Camera Module v1. We used the Raspberry Module. They have a full well capacity of $4.3k$ electrons [20] and a 10-bit analog digital converter (ADC) giving an $e^-/DN$ conversion of approximately 4.2 electrons per digital number. Linearity of the device was confirmed by Belloir et. al. [21], and our own group. The chips were dosed, unbiased, with a continuum of high energy gamma and x-rays created by a linear electron accelerator with a tungsten target. The peak energy of the radiation spectrum was $2\ MeV$. Ionizing radiation is a well-documented underlying cause of RTS behavior that creates defects on the $Si/SiO_2$ interface, including the shallow trench isolation [22]. Frames for all imagers were taken in dark conditions with six second integration times at a temperature of 23℃.

## III - HAAR WAVELET ANALYSIS

### *A. The Discrete Wavelet Transform*

Central to the following RTS noise characterization is the discrete wavelet transform. While there are a variety of suitable wavelets that can be used to perform the transform, here, we will utilize the Haar wavelet. To understand how the discrete wavelet transform works with the Haar wavelet consider a one dimensional vector **f** made of $N$ sampled elements, $(\mathrm{f}_1, \mathrm{f}_2, \mathrm{f}_3, \ldots \mathrm{f}_\mathrm{N})$ such that:

$$\mathbf{f} = (\mathrm{f}_1, \mathrm{f}_2, \mathrm{f}_3, \ldots \mathrm{f}_\mathrm{N}) \tag{1}$$

To perform the wavelet transform we take the raw signal **f** and use it to create two daughter vectors **a** and **d**, each of which are half the length of signal **f** [16]. The **a** series is the trend or average series, and its coefficients are derived from the original signal as a running average such that:

$$a_m = \frac{f_{2m-1}+f_{2m}}{2} \qquad 1 < m \leq N/2 \tag{2}$$

The **d** series is called the details vector and its coefficients track the changes in the original signal similar in function to a derivative:

$$d_m = \frac{f_{2m-1}-f_{2m}}{2} \qquad 1 < m \leq N/2 \tag{3}$$

Since a transform is performed, it is necessary there be an inverse transform as well. For the Haar wavelet transform, the original signal can be recovered as follows:

$$\mathbf{f} = \left(\frac{\mathrm{a}_1+d_1}{2}, \frac{\mathrm{a}_1-d_1}{2}, \ldots \frac{\mathrm{a}_N+d_N}{2}, \frac{\mathrm{a}_N-d_N}{2}\right) \tag{4}$$

It should be noted here that all the coefficients in both the trend and details series are multiplied by $\sqrt{2}$ in order to ensure that the total energy of the signal (the sum of the squares of the samples) is conserved throughout the transform.

A key feature of the wavelet transform is multi-resolution analysis (MRA). It is MRA that allows the wavelet transform to act like a microscope for digital signals, picking out key features at any scale of interest [17]. For example, if one is interested in features that occur on longer time scales it may be beneficial to perform the Haar wavelet transform several times, first to the original signal, then to its trend daughter signal, and so on. Each transform produces a trend and details series half the size of the signal from which they were derived, and therefore each coefficient in subsequent levels represents $2^k$ values from the raw signal, where $k$ is the number of levels.

Now, with all the pieces laid out, we can construct a series of Haar details operators **W** and Haar trend operators **V** which are scalar multiplied with the original signal to create the sets of coefficients. For the first level (highest resolution) analysis:

$$\mathbf{W}_1^1 = \left(\frac{1}{\sqrt{2}}\right)(1, -1, 0, 0, 0, 0, \ldots)$$

$$\mathbf{W}_2^1 = \left(\frac{1}{\sqrt{2}}\right)(0, 0, 1, -1, 0, 0, \ldots)$$

The first level details coefficients are then generated as follows:

$$d_1 = \frac{f_1-f_2}{\sqrt{2}} = \mathbf{f} \cdot \mathbf{W}_1^1$$

$$d_m = \mathbf{f} \cdot \mathbf{W}_m^1$$

Note that the superscript on the operator represents the level of resolution. Therefore, the details operator to find the $m^{th}$ element of the $k^{th}$ level transform is represented as $\mathbf{W}_m^k$.

The trend operators are likewise constructed:

$$\mathbf{V}_1^1 = \left(\frac{1}{\sqrt{2}}\right)(1, 1, 0, 0, 0, 0, \ldots)$$

$$\mathbf{V}_2^1 = \left(\frac{1}{\sqrt{2}}\right)(0, 0, 1, 1, 0, 0, \ldots)$$

Similar to the details coefficients:

$$a_1 = \frac{f_1+f_2}{\sqrt{2}} = \mathbf{f} \cdot \mathbf{V}_1^1$$

$$a_m = \mathbf{f} \cdot \mathbf{V}_m^1$$

### *B. Wavelet Denoising*

The key step in the RTS analysis algorithm is denoising the original signal using the coefficients generated by the discrete wavelet transform (DWT). This method is particularly useful for detecting and characterizing RTS pixels because it suppresses white noise while leaving larger sudden changes untouched. One can think of it as a high-pass or low-pass filter that is dependent on change in magnitude rather than frequency.

As a first step the DWT is performed and the details vector coefficients are examined. If a particular coefficient falls below a specified threshold, it is set to zero. If a coefficient is larger than the threshold, it is either untouched (hard thresholding), or is subtracted by the threshold value (soft thresholding).

This threshold itself can be derived by a variety of techniques. The threshold chosen here is the VisuShrink, or Universal Threshold $T$ defined as [18]:

$$T = \hat{\sigma}\sqrt{2\log(n)} \qquad (5)$$

where $n$ is the number of elements in the discrete signal and $\hat{\sigma}$ is an estimate of the noise equal to the median of the absolute values in the details vector, $median\{\mathbf{d}\}$ divided by $u_{0.75} = 0.6745$, the 0.75 quantile of a normal distribution [18].

Though there are a variety of thresholds to choose from, the Universal Threshold is an ideal choice since it usually underfits the data [18], or in this case, minimizes the number of false RTS events.

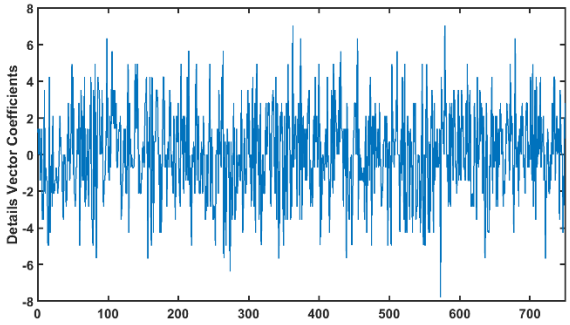


**Figure 2:** A typical details vector before thresholding. It contains half the number of elements as the signal undergoing the transform.

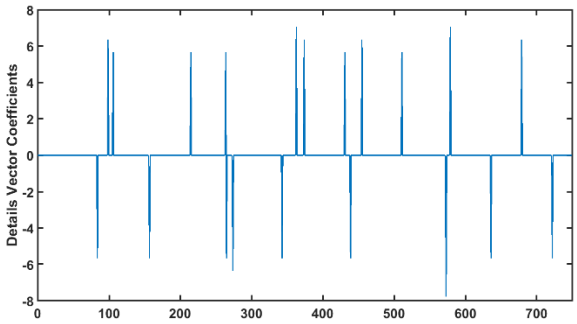


**Figure 3:** A typical details vector after thresholding

Recall that the details vector of the wavelet transform is generated by the changes in the original signal. As seen in figures 2 and 3, thresholding a details vector can greatly simplify, or reduce the noise power in the original signal, making the task of analyzing only the RTS noise far more manageable.

## IV - SIGNAL RECONSTRUCTION

In order to analyze RTS amplitude and time constant distributions in radiation damaged sensors a noise free (RTS exempt) approximation signal is constructed based on the raw output from a particular pixel over several hours. The following process is designed to be highly discriminatory when validating a pixel for exhibiting RTS behavior. This is done to prevent false positive RTS detection from characteristics like high white noise, pink noise, or single events like cosmic ray impacts from polluting the statistics pool.

### *A. Window Comparison*

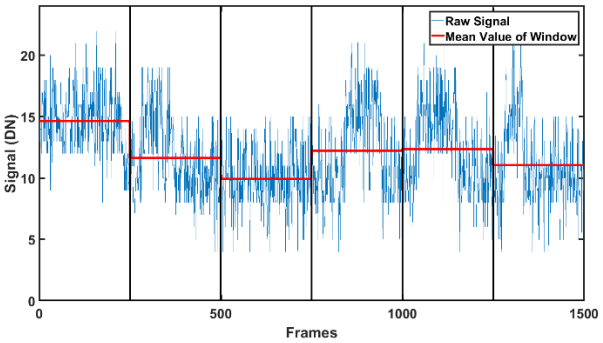


**Figure 4:** Stage 1, the raw signal **f** is split into windows of size 250 frames. The mean values of a window is compared to the mean of the previous two windows.

The first step in the construction process is simply to break up the raw pixel signal into sections and compare the mean values of adjoined sections and their neighbor. This crude but effective RTS-Noise detector uses the standard deviation, $\sigma_r$ of a signal as the metric for RTS candidacy. If the mean value of a particular section is greater or less than the mean value of the previous section by at least $\sigma_r$ the pixel is passed along for analysis. We have chosen here to use six windows representing 250 frames. This first simple step is important to the process not

only because it does very well picking out RTS pixel candidates, but also because it saves precious run time by ensuring the computational heavy lifting is only performed on signals of interest. If a pixel fails the window comparison, the program simply moves on to the next.

*B. DWT Denoising*

A pixel that passes the window comparison test is then run through the DWT denoising process described above. The following analysis utilized a 7-level denoising routine.

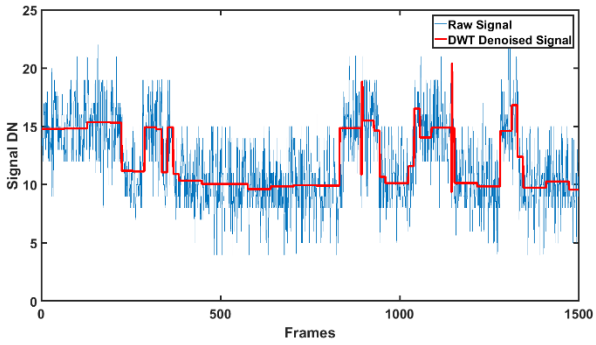


**Figure 5:** Stage 2, the signal f is run through the DWT denoising process, detailed above, and returned as the denoised signal $\mathbf{f}'$. Though the white noise is severly depressed, transient spikes remain.

*C. Temporal Screen*

The denoising process cleans the signal, however issues remain. First, the magnitude of the RTS transition amplitudes in the approximation often fall short of their true value, leaving a systematic error in our reporting. Second, very brief transitions appear in this denoised version, these are ringing artifacts. Since these features often fall outside of the Nyquist limit, they must be disregarded as transients in the characterization. In order to screen these brief transitions from the approximation signal temporal thresholding phase is employed in the program. This is accomplished by simple comparison and is possible because of the nature of the DWT denoising process. As seen in Figure 5, DWT denoising can leave long runs of sequential frames with exactly the same value. This means that in order to verify that a particular transition is not transient, all that is needed is to compare frame $k$ with frame $k-1$. If there is some difference in their values it is understood that a transition has taken place. Then, we compare the value of frame $k$ with the value of the next $l$ frames where $l$ is the width of our temporal screen. If in fact the value of $k$ is the same as the next $l$ frames, the value is kept. If it fails this condition the value of frame $n$ is set to the value of frame $k-1$. The width of this screen can vary and can be subject to debate. On the one hand, the goal should be to construct a signal that is as closely correlated to the original as possible. On the other, many RTS signals display amplitudes that barely exceed the white noise, which can cast doubt on their very existence. In order to further increase the confidence of a transition we have chosen to set $l$ equal to 10.

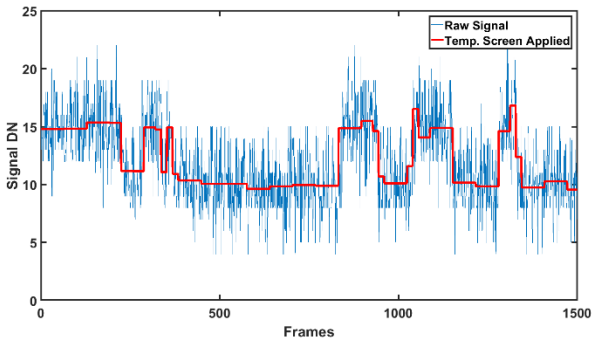


**Figure 6:** Stage 3, the denoised signal $\mathbf{f}'$ is passed through the temporal screen and returned as the denoised and screened signal $\mathbf{f}''$ Transient spikes have been removed.

*D. A Second Thresholding*

At this point the signal shows almost no remnant of the white noise. With the transients removed and the majority of the heavy lifting taken care of by the DWT denoising, all that remains is to again threshold the changes in the screened signal. Recognizing that most of the changes, sample to sample, are zero, and only the largest changes are RTS transitions, the goal is to remove the smaller variations left over from the DWT denoising process. This time, rather than the dyadic DWT, we simply create a new series of size $N-1$ by subtracting each value from the preceding one starting with element two. Here $N$ is, again the number of elements in the signal and $\mathbf{f}'$ is the members of the screened signal. $\mathbf{s}$ is used in place of $\mathbf{d}$ to emphasize the non-dyadic quality of this last details vector.

$$\mathbf{s} = (s_1, s_2, s_3, \ldots f_{N-1}) \tag{6}$$

$$s_m = f'_m - f'_{m-1} \tag{7}$$

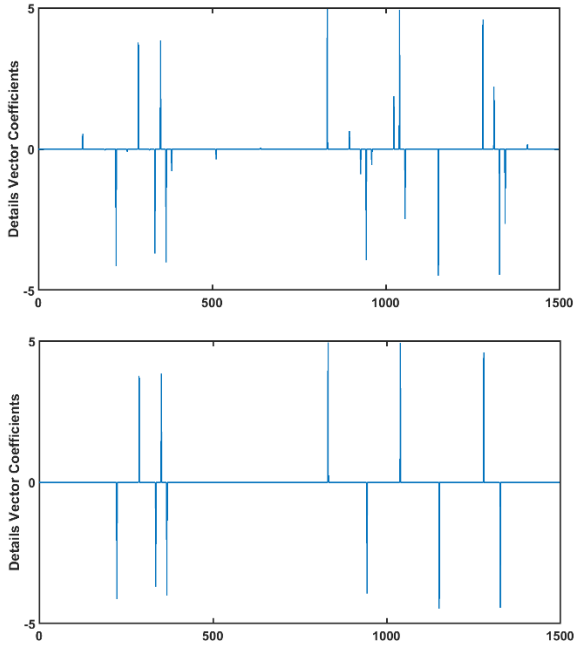


**Figure 7:** Stage 4, a typical details vector before and after denoising. All but a few of the elements are set to zero.

Again, the threshold is applied to this series just as before, but now the threshold is chosen differently. Since there are now so few large changes representing RTS transitions, and some smaller ones left over from the DWT process, we set the threshold $T_s = s_{MAX} * u_{0.75}$ [9]. All elements smaller than the threshold are again set to zero, while those larger are untouched.

*E. Final Reconstruction*

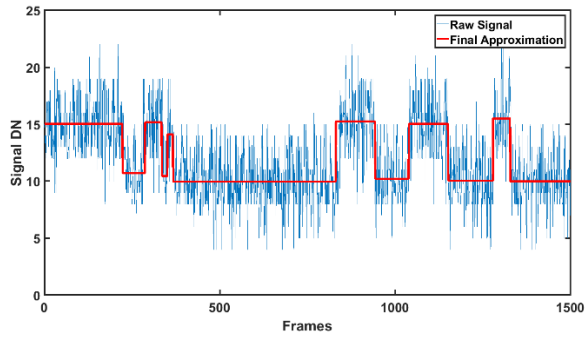


**Figure 8:** Stage 5, The final approximation is constructed. From here RTS transition amplitudes and time constants can be collected for statistical analysis.

For the final reconstruction, the locations of the remaining non-zero elements are taken from the second threshold series, **s** and the mean values of the original signal between those locations are used to fill in the approximation. By using the mean value of the raw signal between transitions, it is ensured that the final amplitudes are very close to the actual values. From this form it is simple to collect time constants and transition amplitudes from tens of thousands of RTS pixels and study them from a statistical perspective.

## V-RESULTS

The semilogarithmic plot of the distribution of maximum RTS transition amplitudes in Figure 9 reveals that, as expected, a larger dose leads to more RTS pixels. The amplitudes observed in this analysis can reach large magnitudes, up to $350e^{-}/s$, though magnitudes of over $10000e^{-}/s$ have been reported [22]. It is notable that the slopes of the curves share a similar shape in all of the semi-log histogram curves, indicating that a higher dose increases the probability of creating a metastability, but the amplitude probability is set.

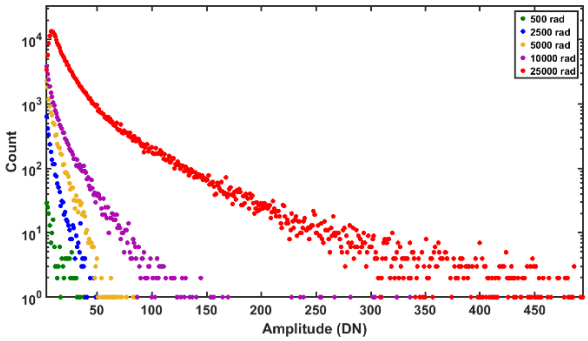


**Figure 9:** The distribution of RTS transition maximum amplitudes

Similar to the maximum amplitude plot, the state lifetime histograms of Figures 10 & 11 display an exponential distribution, though far more flat, here with a peak at approximately 250 frames, or around 85 minutes. It is likely that the shortest transition times are artificially suppressed by choosing to denoise the signals down several levels. A signal that is denoised four levels would yield a high-resolution analysis at the cost of approximation accuracy from false positives. A curiosity from the plots is the apparent flattening of the distribution peak seen in the 'low state' time constants, i.e., the lower of the two level dark current signal levels. This may indicate that the physical configurations that produce the 'low state' for DC-RTS pixels are, on average, more stable than the 'high state' configuration.

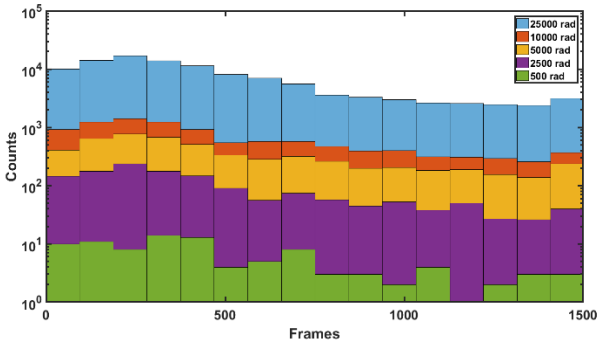


**Figure 10:** The distribution of 'high' state time constants

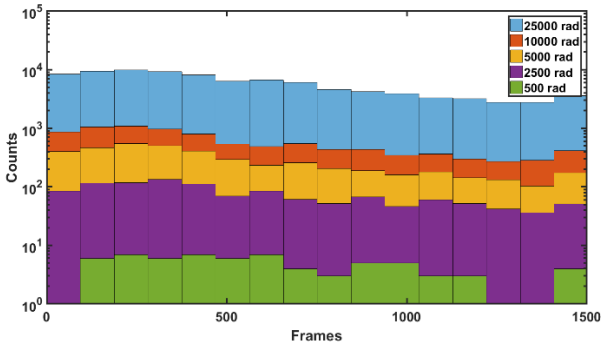


**Figure 11:** The distribution of 'low' state time constants

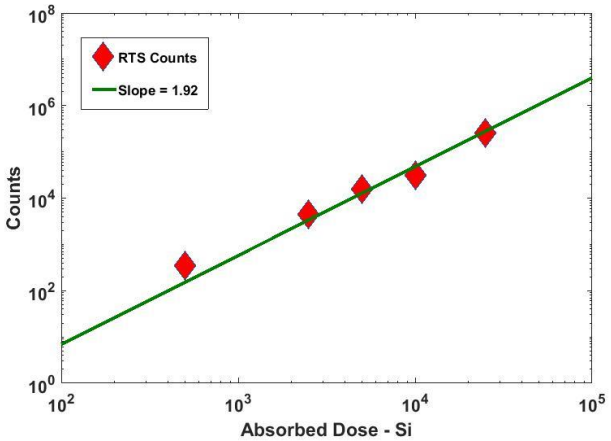


**Figure 12:** The number of RTS pixels as a function of absorbed radiation dose (Rad(Si))

The number of RTS pixels does not follow a linear correlation with radiation dose, but rather increases almost quadratic with the dose. This result indicates that the process creating RTS centers by $\gamma$-radiation is of second-order. There is some precedent for this type of defect generation mechanism. It has been reported that very high doses of $\gamma$-radiation is responsible for the formation of defect centers known as $H\ (97K)$ and $I^{0/-}\ (200\ K)$, designated as such by their peaks on a thermally stimulated current (TSC) spectrum. The $I$ center band energy has been measured at $0.5eV \pm 0.05eV$ below the conduction band, very close to the RTS defect energies reported in [4],[5]. There is some discussion as to whether or not $H$ is simply the donor state of $I$, making them the same defect. Regardless, both states grow in population at a nearly quadratic rate with dose and share nearly the same slope on a log-log plot, as the data reported in Figure 12 [23]. While far from conclusive in identifying the defect responsible for DC-RTS on the interface of pixels, $2^{nd}$ order generation narrows down the field of candidates and provides a potential path toward that identification. For example, the double vacancy oxygen ($V_2O$) complex which can be formed when a $\gamma$-ray strikes a vacancy oxygen defect, i.e., $V + O \rightarrow VO$, then $VO + V \rightarrow V_2O$ is such a candidate.

## VI – CONCLUSION

We report the results of a study into DC-RTS noise in commercial image sensors irradiated with high energy photons. The study utilized a wavelet denoising method that suppresses Gaussian noise while preserving RTS level transitions. That method was explained in detail. We found that while increased dose increases the chances of creating an RTS center, the amplitude probability distribution is independent of dose. Finally, we report that the number of RTS pixels does not increase linearly with dose, but instead the dependence is nearly quadratic. This indicates that the defect responsible for DC-RTS from high energy photons arises from a second order generation mechanism, which provides guidance for further studies in this area.

## REFERENCES

[1] P. L. Leonard and S. V. Jaskolski, "An investigation into the origin and nature of "Popcorn noise"," in *Proceedings of the IEEE*, vol. 57, no. 10, pp. 1786-1788, Oct. 1969.

[2] W. Shockley and W. T. Read, "Statistics of the Recombination of Holes and Electrons," *Phys. Rev*. vol. 87, no. 835, Sep. 1952

[3] R. N. Hall, "Electron-Hole Recombination in Germanium," *Phys. Rev*. vol. 87, no. 387, Jul. 1952

[4] C. Virmontois *et al*., "Total Ionizing Dose Versus Displacement Damage Dose Induced Dark Current Random Telegraph Signals in CMOS Image Sensors," in *IEEE Trans. on Nucl. Sci.*, vol. 58, no. 6, pp. 3085-3094, Dec. 2011.

[5] J. Bogaerts, B. Dierickx and R. Mertens, "Random telegraph signals in a radiation-hardened CMOS active pixel sensor," in *IEEE Trans. on Nucl. Sci.*, vol. 49, no. 1, pp. 249-257, Feb. 2002.

[6] G. R. Hopkinson, "Cobalt60 and proton radiation effects on large format, 2-D, CCD arrays for an earth imaging application," *IEEE Trans. Nucl. Sci.*, vol. 39, pp. 2018–2025, Dec. 1992.

[7] I. H. Hopkins and G. R. Hopkinson, "Random Telegraph Signals from Proton-Irradiated CCDs," *IEEE Trans. Nucl. Sci.*, vol. 40, pp. 1567–1574, Dec. 1993.

[8] I. H. Hopkins and G. R. Hopkinson, "Further Measurements of Random Telegraph Signals in Proton-Irradiated CCDs," *IEEE Trans. Nucl. Sci.*, vol. 42, pp. 2074–2081, Dec. 1995.

[9] V. Goiffon, P. Magnan, P. Martin-Gonthier, C. Virmontois, and M. Gaillardin, "New source of random telegraph signal in CMOS image sensors," presented at the International Image Sensor Workshop, Hokkaido, Japan, 2011.

[10] V. Goiffon, G. R. Hopkinson, P. Magnan, F. Bernard, G. Rolland, and O. Saint-Pe, "Multilevel RTS in Proton Irradiated CMOS Image Sensors Manufactured in a Deep Submicron Technology," *IEEE Trans. Nucl. Sci.*, vol. 56, pp. 2132–2141, Aug. 2009.

[11] G. Chen, W. Xie and Y. Zhao, "Wavelet-based denoising: A brief review," *2013 Fourth International Conference on Intelligent Control and Information Processing (ICICIP)*, Beijing, 2013, pp. 570-574.

[12] Ç. P. Dautov and M. S. Özerdem, "Wavelet transform and signal denoising using Wavelet method," *2018 26th Signal Processing and Communications Applications Conference (SIU)*, Izmir, 2018, pp. 1-4.

[13] P. S. Addison, J. Walker and R. C. Guido, "Time--frequency analysis of biosignals," in *IEEE Engineering in Medicine and Biology Magazine*, vol. 28, no. 5, pp. 14-29, September-October 2009.

[14] Yu-Feng Li, "Image denoising based on undecimated discrete wavelet transform," *2007 International Conference on Wavelet Analysis and Pattern Recognition*, Beijing, 2007, pp. 527-531.

[15] A. Ouahabi, "A review of wavelet denoising in medical imaging," *2013 8th International Workshop on Systems, Signal Processing and their Applications (WoSSPA)*, Algiers, 2013, pp. 19-26.

[16] J. S. Walker, *A Primer on Wavelets and their Scientific Applications*. 2nd ed. Boca Raton [Fla.]: Chapman & Hall/CRC, 2008.

[17] M. Gilli, *Computational Economic Systems: Models, Methods & Econometrics.* Springer Science & Business Media, Mar. 2013.

[18] G.P. Nason “Choice of the Threshold Parameter in Wavelet Function Estimation.” In: Antoniadis A., Oppenheim G. (eds) *Wavelets and Statistics*. *Lecture Notes in Statistics,* vol 103. Springer, New York, NY, 1995

[19] J. Groß*, Linear Regression*. Springer-Verlag Berlin Heidelberg, July 2003.

[20] *OV5647 5-megapixel product brief,* Omnivision, Santa Clara, CA, Nov. 2010.

[21] J. M. Belloir, V. Goiffon, C. Virmontois, P. Paillet, M. Raine, P. Magnan, and O. Gilard, “Dark Current Spectroscopy on Alpha Irradiated Pinned Photodiode CMOS Image Sensors,” *IEEE Trans. Nucl. Sci.*, vol. 63, pp. 2183–2192, Aug. 2016.

[22] E. Martin, T. Nuns, C. Virmontois, J.-P. David, and O. Gilard, “Proton and g -Rays Irradiation-Induced Dark Current Random Telegraph Signal in a 0.18-mm CMOS Image
Sensor,” *IEEE Trans. Nucl. Sci.*, vol. 60, pp. 2503–2510, Aug. 2013.

[23] I. Pintilie, E. Fretwurst, G. Lindström, J. Stahl, “Second-order generation of point defects in gamma-irradiated float-zone silicon, an explanation for ‘type inversion’,” *Applied Physics Letters*, vol. 82, pp. 2169-2171, Mar. 2013.